Longitudinal in vivo Ca^{2+} imaging reveals dynamic activity changes of diseased retinal ganglion cells at the single-cell level

Liang Li[a,1] (ID), Xue Feng[a,1] (ID), Fang Fang[a,b,1], David A. Miller[c] (ID), Shaobo Zhang[d], Pei Zhuang[a], Haoliang Huang[a], Pingting Liu[a] (ID), Junting Liu[a] (ID), Nripun Sredar[a], Liang Liu[a] (ID), Yang Sun[a], Xin Duan[d], Jeffrey L. Goldberg[a], Hao F. Zhang[c] (ID), and Yang Hu[a,2] (ID)

Retinal ganglion cells (RGCs) are heterogeneous projection neurons that convey distinct visual features from the retina to brain. Here, we present a high-throughput in vivo RGC activity assay in response to light stimulation using noninvasive Ca^{2+} imaging of thousands of RGCs simultaneously in living mice. Population and single-cell analyses of longitudinal RGC Ca^{2+} imaging reveal distinct functional responses of RGCs and unprecedented individual RGC activity conversions during traumatic and glaucomatous degeneration. This study establishes a foundation for future in vivo RGC function classifications and longitudinal activity evaluations using more advanced imaging techniques and visual stimuli under normal, disease, and neural repair conditions. These analyses can be performed at both the population and single-cell levels using temporal and spatial information, which will be invaluable for understanding RGC pathophysiology and identifying functional biomarkers for diverse optic neuropathies.

Ca^{2+} imaging | retinal ganglion cell | glaucoma | single cell | in vivo

Retinal ganglion cells (RGCs) are the only projection neurons in the retina, responsible for collecting all visual information processed by other retinal neurons and relaying that information through the optic nerve to the brain (1, 2). The optic nerve is highly vulnerable to optic neuropathies (3–6), in which injury or diseases cause characteristic progressive RGC death and optic nerve degeneration. Glaucoma is the major optic neuropathy and the leading cause of irreversible blindness (7, 8). Although it is to some extent treatable, glaucoma is called a "silent killer of vision", because it is often diagnosed at a very late stage when neurodegeneration is already advanced. Therefore, early detection of RGC morphological and functional glaucomatous changes is critical to prevent irreversible loss of vision. Similarly, to evaluate the efficacy of neuroprotective and regenerative therapies, there exists a significant need to monitor RGC morphology and function longitudinally to properly assess the time course of disease progression. Visual field mapping is a clinical standard to evaluate glaucoma, but it complicates diagnosis and detection of progression because it is highly variable and fails to monitor RGC function directly (9–15). Pattern electroretinogram (PERG) offers an electrophysiological assessment of populations of RGCs in living animals (16–18). The variation of PERG signal is rather large, however, and we and others found that, although PERG is sensitive to optic nerve injury, its deficits do not correlate well with the progression of RGC degeneration in either rodents or large animals (19–24). Additionally, RGCs are heterogeneous: based on their diverse morphological, molecular, and physiological characteristics, and in adult mouse, they are classified into 46 types with distinct molecular signatures (1, 25). Current in vivo functional assays only provide overall RGC activities without cellular resolution, a major unmet need.

Ex vivo electrophysiological recording of individual RGCs, especially multi-electrode array (MEA) (26–28), is a highly efficient approach to acquire RGC activity in response to visual stimuli; MEAs have defined more than 30 functional RGC types in the mouse retina (1, 2, 29–34). Alternatively, neuronal activity can be optically monitored by Ca^{2+} imaging because synaptic response and action potential firing normally evoke rapid changes of intracellular free calcium. Furthermore, the dynamic change of intracellular Ca^{2+} levels is coupled to the electrical properties of the neuron, thus faithfully reflecting neuronal activity (35). Therefore, genetically encoded Ca^{2+} indicators (GECIs) have been extensively used as a surrogate measurement of neuronal activity (36–38). Ca^{2+} imaging of isolated retinal patches loaded with fluorescent Ca^{2+}-sensitive dye or infected with GECI can define clusters of functional RGCs that faithfully correlate with ex vivo electrophysiological characteristics of mouse RGCs (39, 40). However, the ex vivo method may generate artifacts, and it does not permit longitudinal recording of the same RGCs during degeneration or in response to treatment.

Significance

Here, we present a proof-of-concept study that establishes a high-throughput in vivo imaging strategy to measure the light-evoked neuronal activities of thousands of retinal ganglion cells (RGCs) simultaneously and noninvasively. By taking advantage of the superb optical accessibility of the mouse eye and the power of cSLO/GCaMP-mediated Ca^{2+} imaging, we directly visualize RGC activities in response to visual stimulations for up to several weeks and develop and validate powerful analytic protocols. This technique allows us to appreciate the striking dynamic functional changes of RGCs at both population and single-cell levels under normal, traumatic, and glaucomatous conditions. Future development and broader applications of this technique in the future will provide highly informative and insights into RGC physiology and pathology.

[1]L.L., X.F. and F.F. contributed equally to this work.

[2]To whom correspondence may be addressed. Email: huyang@stanford.edu.

Due to the superb optical accessibility of retina, fluorescence-labeled RGCs can be imaged noninvasively in living animals by confocal scanning laser ophthalmoscopy (cSLO) (41–43). Earlier studies also demonstrated the feasibility of in vivo Ca^{2+} imaging in the mouse retina using adaptive optics (AO)-SLO (44, 45). Therefore, we employed cSLO customized with light stimulation and jGCaMP7s, a GECI with high signal-to-noise ratio (46), to optically record light-evoked activities of ~1,200 RGCs/retina simultaneously in living animals. More than 40 RGC clusters were recognized by unsupervised algorithms initially and then hierarchically regrouped into nine activity groups with distinct ON, OFF, and ON–OFF dynamic responses to ultraviolet (UV) light stimulation. Using this in vivo neuronal activity readout, we longitudinally characterized the dynamic functional changes of RGCs at both population and single-cell levels in two optic neuropathy models: acute optic nerve crush (ONC) (47–49) and chronic silicone oil–induced ocular hypertension/glaucoma (SOHU) (21, 23, 24). These studies reveal for the first time distinct functional responses of RGCs and unprecedent individual RGC activity conversions during traumatic and glaucomatous degeneration. This proof-of-concept study establishes the foundation for future more advanced studies, such as in vivo RGC functional classification, longitudinal high-throughput evaluation, and neuronal function/ activity conversion detection in broader CNS neuron types.

Results

Establishing the SLO System and Protocol for in vivo RGC Ca^{2+} Imaging. To monitor RGC activity in vivo, we generated AAV2–mSncg–jGCaMP7s to express a GECI with high signal-to-noise ratio (46) in RGCs, driven by an RGC-specific mSncg promoter that we recently identified (50). AAV2–mSncg can drive transgene expression in more than 80% RGCs after intravitreal injection (50), similar to the targeting efficiency of AAV2–mSncg–jGCaMP7s (Fig. 1 *A* and *B*). Because ~95% mouse cones express both middle-wavelength (508 nm) and short-wavelength (360 nm) opsins (M/S ratio is ~1/3) in a dorsal-to-ventral gradient (51–54), short-wavelength UV light can be used as a visual stimulus to activate most mouse cones when green light is used for Ca^{2+} imaging (44, 45, 51). We customized a Heidelberg cSLO by incorporating a mouse holder and an UV light source (395 nm) to allow us to synchronize pan-retina light stimulation with fluorescent fundus imaging (*SI Appendix*, Fig. S1*A*). The 488 nm excitation light used for GCaMP imaging can also excite photoreceptors. However, previous studies have demonstrated that constant excitation laser light plateaus the RGC GCaMP signal (44, 45) and allows detection of additional neuronal activities in response to stimulating light (39, 55). We verified that the same steady states were achieved within 20 s in our system and maintained under constant 488 nm light (*SI Appendix*, Fig. S1*B*). More importantly, adding UV light stimulation during the steady state in the presence of the constant 488 nm imaging light generated characteristic light-evoked ON- or OFF-RGC responses (*SI Appendix*, Fig. S1*C*). Because 20-s UV stimulation generates larger Ca^{2+} signals and captures the dynamics of jGCaMP7s signals in RGCs better than 0.5- or 4-s UV stimulation, we used 20-s UV stimulation in the following experiments, although RGC responses to higher frequency light stimuli (0.5 or 1 Hz) can be readily detected (*SI Appendix*, Fig. S1*D*). Thus, we determined the in vivo imaging protocol of RGC Ca^{2+} signals in response to UV light stimulation: turn on the 488 nm imaging light for at least 20 s before the 60 s recording procedure (the longest duration for video recording allowed by the Heidelberg SLO) and then record 10 s before UV stimulation to get the basal level of fluorescence

(*F0*), 20 s of UV illumination, and 30 s after UV offset to obtain stimulation (ON or OFF)-induced fluorescence (*F*) (Movie S1). This protocol allows us to visualize many RGCs simultaneously with reasonable temporal frequency (4.7 frames/s) and track the response dynamics of the same RGCs over weeks.

We then recorded movies of jGCaMP7s fluorescent signals in naïve mouse retinas within an eccentricity of 55°. Fluorescent signals were extracted from each detectable RGC within each retinal quadrant (nasal, temporal, dorsal, and ventral) with an average of ~1,200 RGCs/retina. The mean time-dependent fluorescent signal from each RGC (*F*) was normalized by subtracting the mean pre-stimulus signal intensity (F0), which can be expressed as $\Delta F = F - F0$. The normalized neuronal responses ($\Delta F/F0$) of each RGC were then automatically calculated (Fig. 1*C*). We confirmed that peripheral ventral RGCs responded to UV light stimulation much more vigorously than peripheral dorsal RGCs (*SI Appendix*, Fig. S1*E*), consistent with the dorsal–ventral gradient S-opsin distribution in the B6 mouse retina (54). However, in the fundus region that we routinely imaged (over an eccentricity of 55° surrounding the optic nerve head), the ventral and dorsal RGCs showed no significant difference in response to UV light (*SI Appendix*, Fig. S1*F*), probably because of similar S-opsin distribution across this region (54). To determine the range of non-specific RGC fluorescence changes caused by the imaging procedure but unrelated to Ca^{2+} levels or UV stimulation, we performed two control recordings from: 1) AAV–mSncg–GFP labeled RGCs in response to UV stimulation and 2) AAV–mSncg–jGCaMP7s labeled RGCs without UV stimulation. Because these control recordings showed that the average changes of nonspecific fluorescence were within –20 to +15%, we arbitrarily defined the RGCs within this range as NR (no-response) RGCs and only clustered the responsive RGCs beyond this range (Fig. 1 *D* and *E*). We then analyzed the responding 8,998 RGCs from eight naïve retinas with significant changes in fluorescence intensity in response to UV stimulation using unbiased sparse principal component analysis (sPCA) (56, 57) and the Bayesian information criterion (BIC) analysis (58). We found that with the use of six sPCA features, the BIC analysis generated the optimal 40 clusters (Fig. 1*F*).

Hierarchical Clustering Identifies Nine Groups of RGCs with Characteristic Light-Evoked in vivo Activities. Based on the correlation distance, we further grouped the 40 RGC clusters into nine activity groups by a customized one-dimensional hierarchical clustering MATLAB script (Fig. 2 *A* and *B*), similar to the previously described analysis in an ex vivo RGC Ca^{2+} imaging study (39). We also borrowed the ON/OFF nomenclature from ex vivo RGC functional studies to classify in vivo RGC activities. However, it is important to note that the in vivo light-evoked RGC activities determined by Ca^{2+} imaging cannot be directly correlated with RGC functional types defined by ex vivo electrophysiological characteristics. Among the nine groups, there were four groups of ON-RGCs (increase Ca^{2+} signals at the onset of UV light) that included ON-Sustained1–3 (ON-Sust1–3) and ON-Transient (ON-Trans), ON–OFF-RGCs (increase Ca^{2+} signals at both the onset and offset of UV light), and two groups of classical OFF-RGCs (increase Ca^{2+} signals at the offset of UV light) that included OFF-Trans and OFF-Sust, and two groups of OFF-Sustained Suspect RGCs (OFF-SS1 and OFF-SS2, decrease Ca^{2+} signals at the onset of UV light but increase Ca^{2+} signals at the offset, with high baseline activities). Similarly behaving RGCs have been reported in a previous ex vivo study, which named them "OFF-Sustained RGCs" with a high baseline firing rate under steady illumination (33). To differentiate these groups of
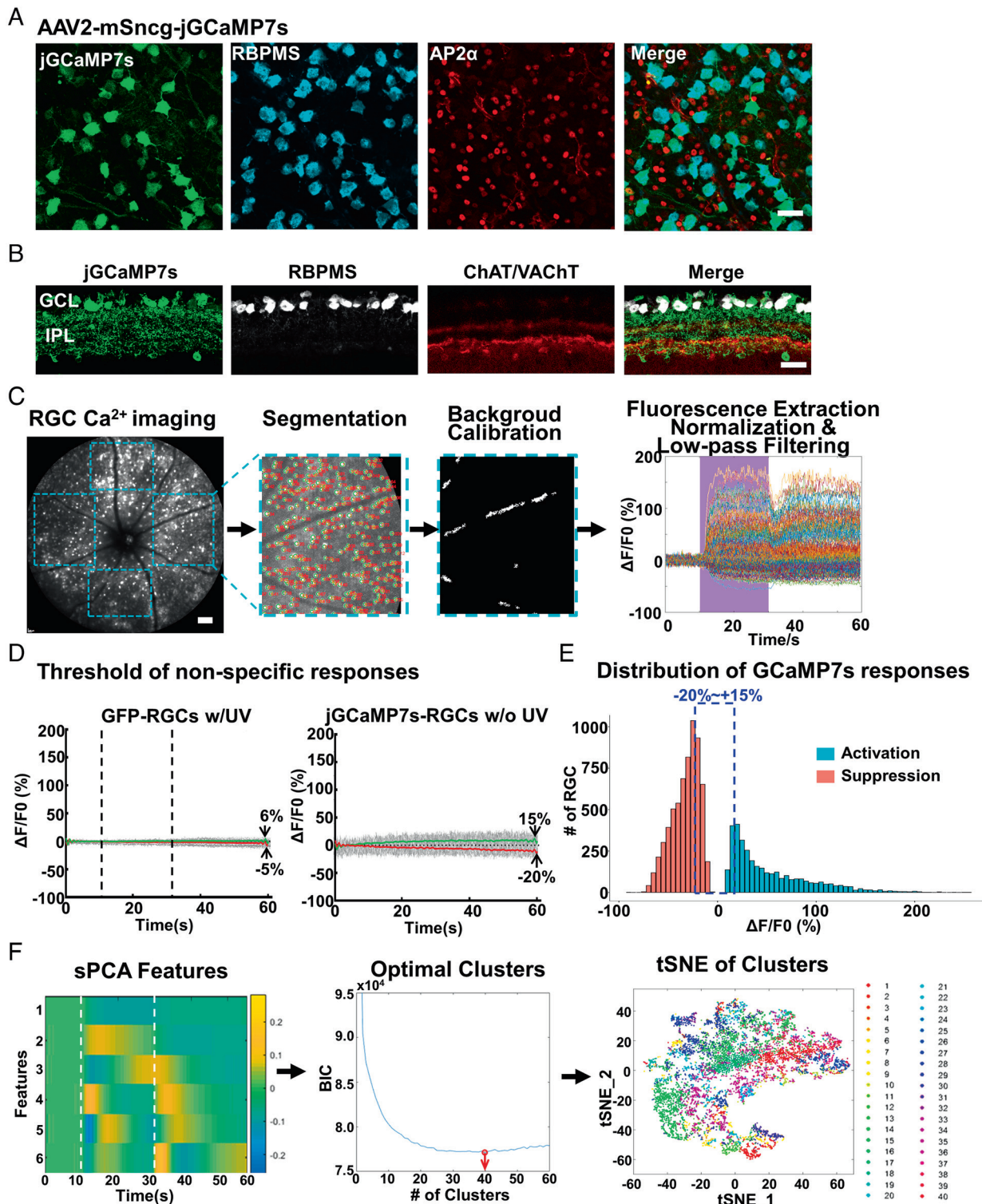
Fig. 1. In vivo Ca^{2+} imaging of jGCaMP7s-labeled RGCs with cSLO in response to light stimuli. (*A* and *B*) Confocal images of retinal wholemounts and sections showing that jGCaMP7s is specifically expressed in RBPMS$^+$ RGCs after intravitreal injection of AAV2−mSncg−jGCaMP7s but not in amacrine cells labeled with AP2α or ChAT/VAChT antibodies. (Scale bar, 20 μm.) The jGCaMP7s signal was augmented by anti-GFP antibodies. GCL (ganglion cell layer), IPL (inner plexiform layer). (*C*) The process of RGC Ca^{2+} imaging and data analysis by customized MATLAB script RSE. From *Left* to *Right*: 60-s-long video (10 s baseline, 20 s of UV stimulation, and 30 s after UV offset) of raw Ca^{2+} imaging from the fundus of mouse retinas infected with AAV2−mSncg−jGCaMP7s; the 624 × 680 μm in the nasal and temporal quadrants and the 624 × 567 μm in the dorsal and ventral quadrants of the retinal fundus were selected for cell segmentation, background calibration with the blood vessel fluorescence, and RGC fluorescence signal extraction; the low-pass filtered and normalized signals were used to generate the light-evoked individual RGC responses (ΔF/F0) as a function of time. (Scale bar, 100 μm.) The purple area indicates the duration of UV stimulation. n = 294 RGCs from the temporal quadrant of one retina. (*D*) The threshold of nonspecific RGC responses was determined by GFP-labeled RGCs (*Left*) in response to a UV stimulus; jGCaMP7s-labeled RGCs without a UV stimulus (*Right*); the gray traces are fluorescence changes (ΔF/F0) of individual RGCs; the green line is the average of the gray traces with ΔF/F0 > 0, and the red line is the average of the gray traces with ΔF/F0 < 0. The lowest point on the red line to the highest point on the green line is −5 to +6% in the GFP RGCs (*Left panel*) and −20 to +15% in the jGCaMP7s RGCs (*Right panel*). n = 1,491 RGCs; dashed vertical lines indicate the ON- and OFF-set of UV stimulation. (*E*) The distribution of light-evoked Ca^{2+} responses (ΔF/F0) of RGCs (divide in X-axis is 5%): The RGCs with Ca^{2+} responses within the range of −20 to +15% are categorized as no-response RGCs. n = 11,247 total RGCs from eight retinas. (*F*) *Left* to *Right*: six sPCA temporal features of RGCs; the BIC curve indicates the optimal number of clusters (40) pointed to by the red arrow; tSNE demonstration of the 40 RGC clusters. n = 8,998 responding RGCs from eight retinas.
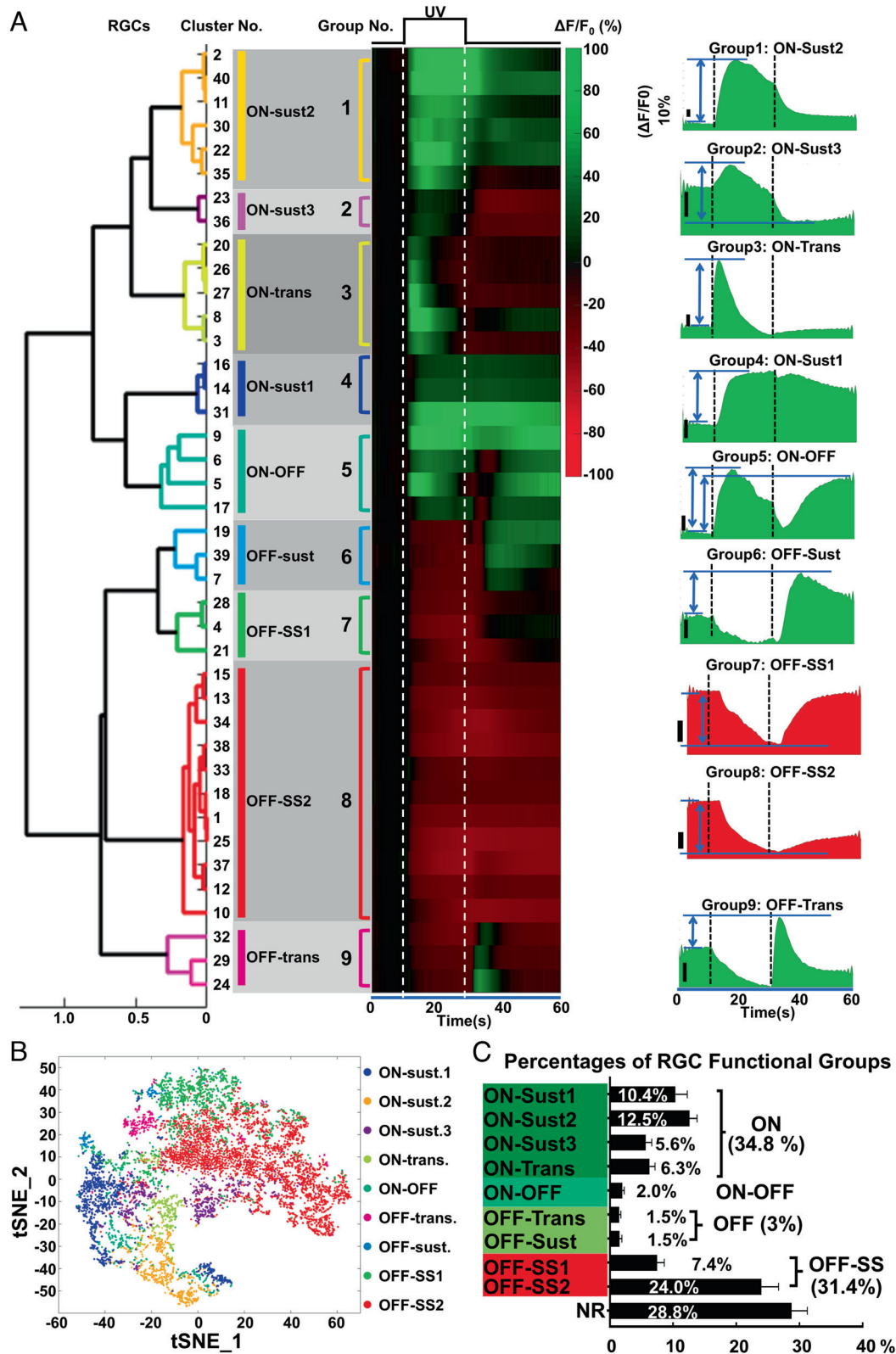
Fig. 2. The nine characteristic light-evoked RGC responses in naïve mouse retinas. (*A*) *Left*: The one-dimensional hierarchical tree and the heatmap of the 40 RGC clusters are shown as the order of groups 1–9. Heatmaps show the uniform responses (ΔF/F0) of each RGC group to the light stimulation: green is activation, and red is suppression. *Right*: the waveforms of nine RGC functional groups: ON-Sust1, ON-Sust2, ON-Sust3, ON-Trans, ON–OFF, OFF-Trans, OFF-Sust, OFF-SS1, and OFF-SS2. The activity (amplitude) measurement of the corresponding RGC groups is indicated with the double-headed arrows in between two horizontal lines. (The vertical dark scale bar, 10%.) The white or black dashed vertical lines indicate the ON/OFF-set of UV stimulation. n = 8,998 RGCs from eight retinas. (*B*) The tSNE map showing the nine RGC functional groups. (*C*) The percentages of individual RGC activity groups and the summed percentages of ON, OFF, ON–OFF, OFF-SS, and NR RGCs from a total of 19 naïve retinas. n = 22,317 RGCs.

OFF-Sustained RGCs from classical OFF-Sustained RGCs, we named them "OFF-Sustained Suspect." Representative videos of single-RGC Ca²⁺ imaging from each of these nine groups and NR RGCs are presented in Movie S2. By referencing these nine activity groups, 15,890 RGCs from 19 naïve retinas were assigned to the individual group with the highest cross-correlation value. There were ~34.8% ON-RGCs, ~3% classical OFF-RGCs, ~31.4% suspected OFF-RGCs, and ON–OFF-RGCs (2.0%) in addition to 6,427 NR RGCs (28.8%, fluorescence changes within +15% to –20%) (Fig. 2C). The low percentage of classical OFF-RGCs agrees with a previous ex vivo MEA study (59), which undersamples the OFF-cells. The actual OFF-RGC percentage is higher, as shown in another MEA study (60). One study using single-electrode recording found that 44% of 87 cells in the mouse retina to be OFF-RGCs (61). The total percentage of classical and suspected OFF-RGCs from our study is close to this number. Therefore, the suspected OFF-RGCs detected in this in vivo setting may well be classical OFF-cells that can be detected under more optimum in vivo imaging/visual stimulation conditions. In summary, we demonstrated the feasibility of in vivo RGC Ca²⁺ imaging and RGC light-evoked activity characterization under physiological conditions in living animals. Next, we used this in vivo readout to evaluate RGC activities longitudinally.

Longitudinal Ca²⁺ Imaging of Naïve RGCs Finds No Significant Changes of Light-Evoked RGC Activities Over Time. We previously demonstrated that AAV–mSncg–mediated transgene expression in RGCs attains stable expression around 4 wk after intravitreal injection (50). We obtained the initial RGC Ca²⁺ imaging dataset (baseline) 4 wk after AAV injection (4 wpi) and then imaged the same group of animals 2, 3, and 7 wk later to evaluate the longitudinal changes of RGC activities. The nine RGC activity groups were readily detectable at each time point, and there was no obvious difference among these time points (Fig. 3 A and B and SI Appendix, Fig. S2A). In addition to the population analyses, our in vivo Ca²⁺ imaging protocol also enabled us to optically follow the same RGCs longitudinally. Software-mediated automatic single-RGC registration and demixing were not reliable. Instead, we manually recognized the same RGCs in Ca²⁺ imaging frames at different time points based on their location and distance to blood vessel markers (SI Appendix, Fig. S2B). We sampled 152 RGCs from six retinas for single-RGC longitudinal tracing from baseline to 7 wk and found that the majority of RGCs kept their original light-evoked activities over time, and very few RGCs changed their original ON activities to OFF activities 7 wk later (Fig. 3 C–E). This critical control experiment demonstrated the reliability of the in vivo RGC Ca²⁺ imaging, which we therefore used with confidence to evaluate the longitudinal functional changes of injured and diseased RGCs in vivo. However, through careful examination, we found that there were ~12% RGC loss at 11 wpi compared to naïve retinas (SI Appendix, Fig. S2C), suggesting that jGCaMP7s overexpression was mildly toxic to RGCs in the long term.

Population Analysis of Longitudinal Ca²⁺ Imaging Reveals Distinct, Dynamic Changes of RGC Activities in ONC and SOHU Glaucoma Models. Traumatic optic nerve injury can be replicated in a mouse by ONC, which lesions all the RGC axons and causes severe RGC soma and axon degeneration, as well as visual function deficits (SI Appendix, Fig. S3 A–D). In contrast to acute traumatic optic nerve injury, glaucoma is a chronic optic neuropathy often associated with elevation of intraocular pressure (IOP) (4, 62). We recently developed a SOHU mouse model with stable IOP elevation and progressive glaucomatous neurodegeneration

(SI Appendix, Fig. S3 E–I) (21, 23, 24), faithfully resembling human pupillary blocking glaucoma caused by surgical use of SO (63, 64). The ONC model is extensively used as a surrogate glaucoma model based on the assumption that the responses of RGCs to traumatic axon injury and IOP elevation–induced axon injury are similar. However, there is clear difference in RGC gene expression in response to traumatic optic nerve injury and glaucoma (65). Here, we systematically compared RGC activity changes under these two conditions.

We took the unique opportunity provided by in vivo RGC Ca²⁺ imaging to directly compare the RGC longitudinal functional changes in response to trauma and glaucoma. We imaged the same groups of animals at multiple time points after ONC or SO injection. Population analyses of longitudinal Ca²⁺ imaging revealed dramatic, dynamic changes of RGC light-evoked activities under traumatic and glaucomatous conditions. Surprisingly, at early time points after ONC but before significant RGC death, 1 and 3 d postcrush (1 and 3 dpc), ON-RGC responses, including total ON-RGC numbers and total ON activities, increased (Fig. 4 A, C, and E). Through close examination of individual RGC activity groups (SI Appendix, Fig. S4), we found that ON-Sust3 RGCs increased significantly, but other ON-RGCs (ON-Sust1/2 and ON-Trans) maintained the same activity level at 1 and 3 dpc. All ON-RGC responses decreased sharply at later time points during which dramatic RGC loss occurs (5–14 dpc) and were almost completely gone at 14 dpc (Movie S3). The total OFF-RGC responses decreased gradually (Fig. 4 C and E), primarily due to steady changes of OFF-SS1/2 RGCs, although a striking loss of OFF-Trans and OFF-Sust RGCs occurred at 3 dpc (SI Appendix, Fig. S4A). In contrast, the functional responses of glaucoma RGCs distinctly differ from those to traumatic optic nerve injury. After SO injection and IOP elevation, all nine RGC activity groups gradually decreased, correlating with milder and slower glaucomatous RGC death, although ON-RGC responses were preserved better than OFF-RGC activities (Figs. 4 B, D, and F and SI Appendix, Fig. S4B and Movie S3). Taken together, longitudinal RGC Ca²⁺ imaging revealed two phases of ON-RGC response to traumatic optic nerve injury: an initial increase in activity followed by a rapid loss later in addition to early loss of ON–OFF, OFF-Trans, and OFF-Sust responses. In contrast, in the SOHU glaucoma model, ON-RGC responses were relatively well preserved, and selective loss of ON–OFF, OFF-Trans, and OFF-Sust responses did not occur.
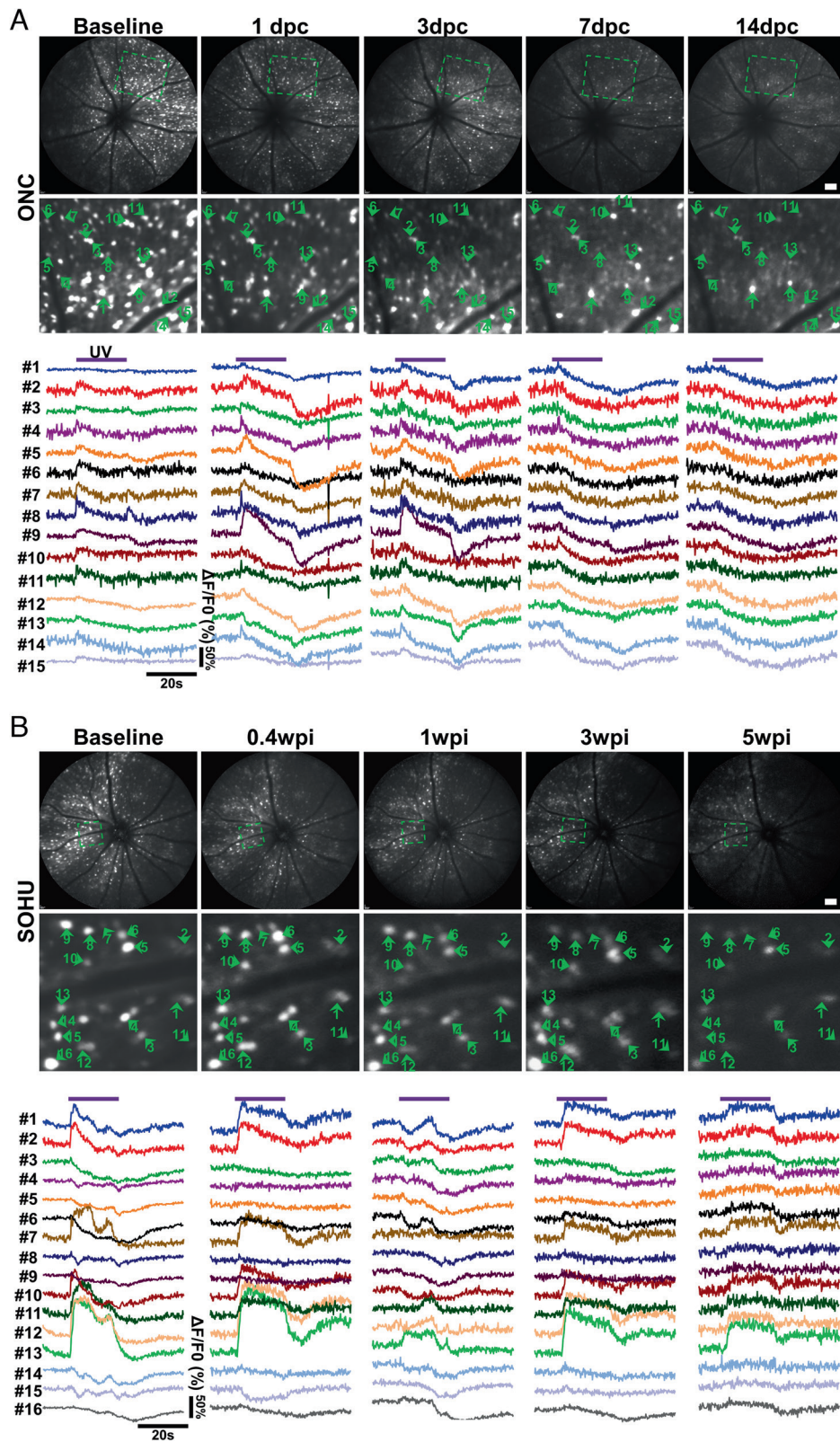
Single-RGC Longitudinal Tracing Reveals Unique Activity Conversions in Response to ONC or Glaucoma. In addition to the population analyses, we also performed longitudinal optical tracing of individual RGCs at different time points after ONC or SO injection. Longitudinal single-RGC tracing in the diseased retina is much more difficult than that in the naïve retina because of significant cell loss. Therefore, in addition to the blood vessel marker, we also included several cells surrounding the target cell as reference; the unique pattern formed by the target cell, blood vessels, and reference cells enabled us to definitively locate the target cell in different images at different time points (SI Appendix, Fig. S5). We first manually recognized 217 surviving RGCs at a late stage (14 dpc) in the ONC model and 534 surviving RGCs at 5 wpi in the SOHU glaucoma model and then retrogradely identified the same cells at earlier time points (Figs. 5 and 6). Surprisingly, in contrast to previous assumptions, RGC activity identities were not static and showed vibrant, unique conversions under different disease conditions. The light-evoked activities of many RGCs transformed several times after ONC. For example, at early time points (1 and 3 dpc), single-RGC tracing of light-
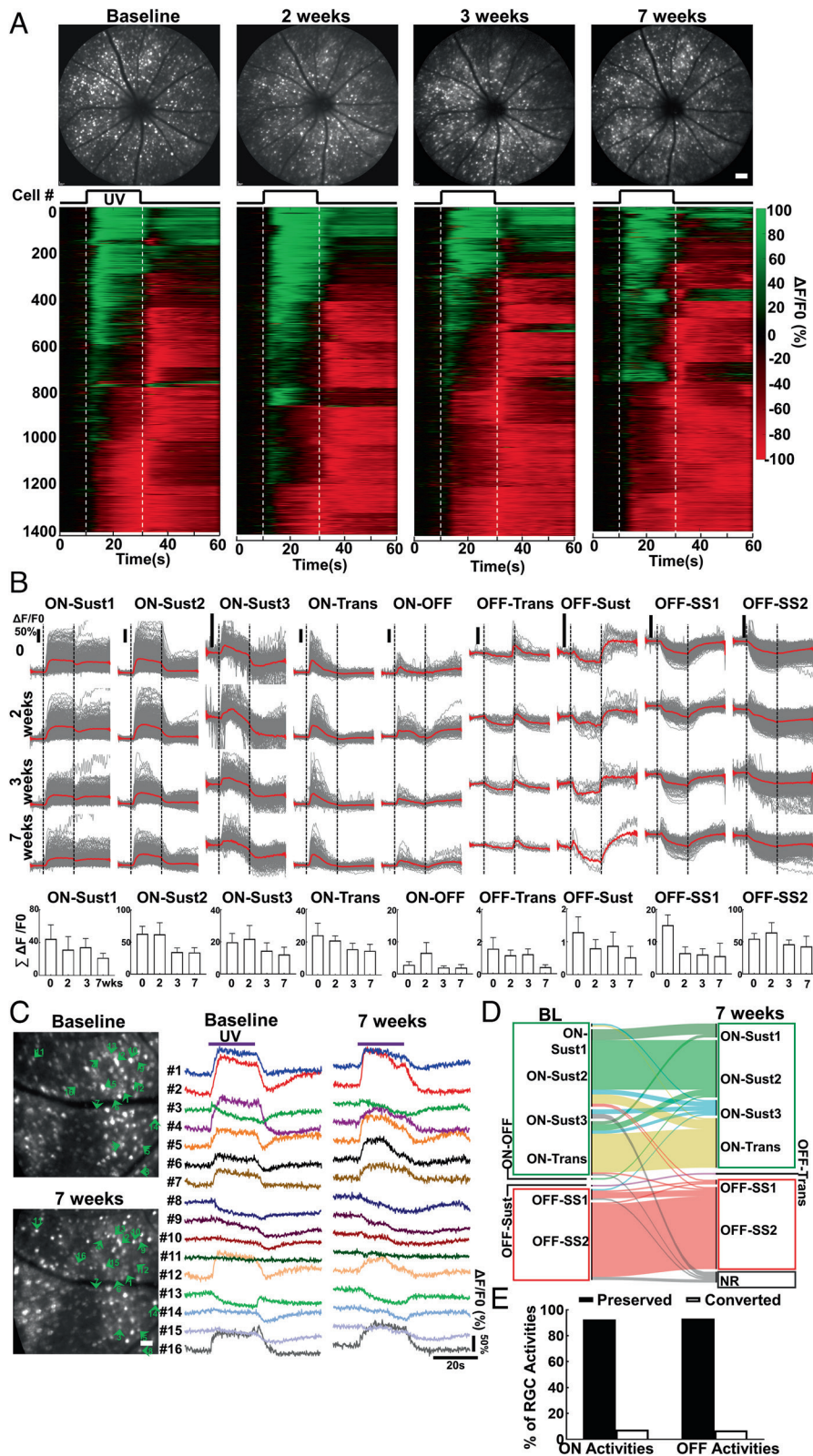
Fig. 3. Longitudinal Ca^{2+} imaging reveals stable light-evoked RGC activities in naïve mice. (*A*) *Upper panel*, representative cSLO fundus images of the same animal at imaging time points 0, 2, 3, and 7 wk. (Scale bar, 100 μm.) *Lower panel*, heatmap of light-evoked activities (ΔF/F0) of all the RGCs from the same retina: green is activation, and red is suppression. (*B*) The gray traces of waveforms are the light-evoked individual RGC response (ΔF/F0) as the function of time for each RGC functional group, and the red line is the mean. Total activities of the individual RGC group expressed as the sum of the corresponding group of RGC amplitudes from each animal. Data are presented as means ± SEM, n = 6 retinas. (*C*) Representative Ca^{2+} imaging of the same area of a naïve retina at baseline (4 wpi) and 7 wk (11 wpi) and comparison of single RGC activities. (*D*) Alluvial map showing a total of 152 RGCs from six retinas sampled for longitudinal analysis of single RGC activities from baseline to 7 wk. (*E*) The percentages of RGCs preserving or changing their original activities over a 7-wk period.
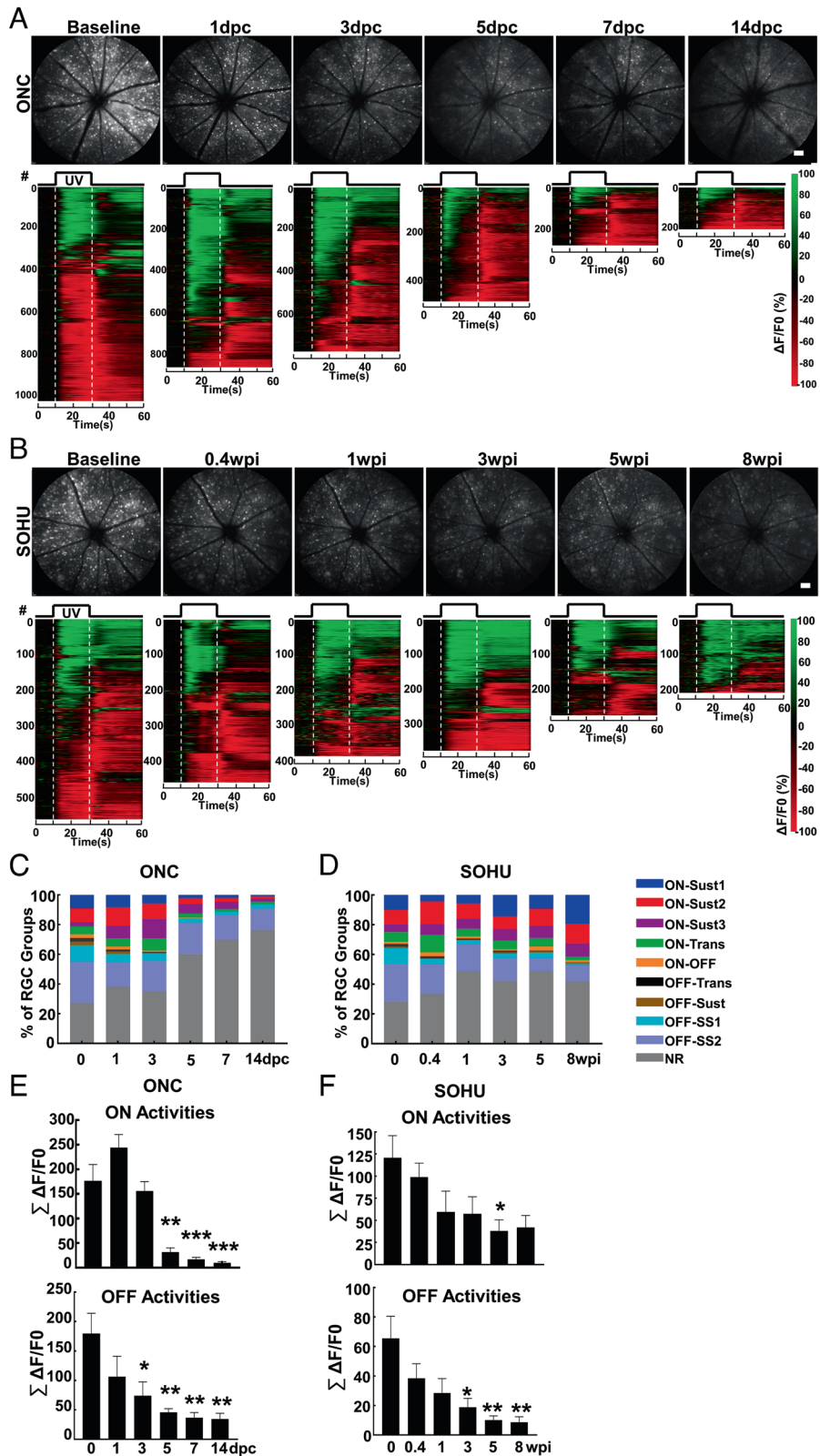
Fig. 4. Population analysis of longitudinal Ca^{2+} imaging reveals markedly different changes in RGC activity in response to trauma and glaucoma. (*A* and *B*) *Upper panel*, representative cSLO fundus images of the same animal at 0, 1, 3, 5, 7, and 14 dpc (days postcrush) or 0, 0.4, 1, 3, 5, and 8 wpi (weeks post-SO injection). (Scale bar, 100 μm.) *Lower panel*, heatmap of light-evoked activities (ΔF/F0) of all the RGCs from the same retina: green is activation, and red is suppression. (*C* and *D*) Percentages of nine RGC activity groups at different time points in ONC or SOHU models detected by longitudinal Ca^{2+} imaging and clustering. n = 8 retinas in ONC and n = 6 retinas in SOHU. (*E* and *F*) Total activities of the ON-RGCs (ON-Sust1–3 and ON-Trans) and OFF-RGCs (OFF-Trans, OFF-Sust, and OFF-SS1/2) at different time points in ONC or SOHU models expressed as the sum of all the ON- or OFF-RGC amplitudes from each retina. Data are presented as means ± SEM, n = 8 retinas in ONC and n = 6 retinas in SOHU. *P < 0.05, **P < 0.01, and ***P < 0.001, one-way ANOVA with Tukey's multiple comparison test.

Fig. 5. Single-cell longitudinal tracing reveals dynamic light-evoked activity transformations of RGCs in response to traumatic injury or glaucoma. (*A*) Representative Ca²⁺ imaging of the same area of the retina at different time points after ONC was used to sample the dynamic changes of light-evoked activities of each RGC functional group. Cells 1, 3, and 15 convert from NR at baseline into ON-RGCs at 1 and 3 dpc and then into OFF-SS RGCs at late time points (7 and 14 dpc). Cells 2, 5, 9, and 14 first increase ON activities at 1 and 3 dpc and then also convert to OFF-SS RGCs at late time points (7 and 14 dpc). Cell 8 converts from ON–OFF at baseline into ON-RGC at 1 and 3 dpc and then into OFF-SS RGC at late time points (7 and 14 dpc). Cells 12 and 13 convert from OFF-SS RGCs at baseline into ON-RGCs at 1 and 3 dpc and then change back to OFF-SS RGCs at late time points (7 and 14 dpc). Cells 4, 6, 10, and 11 keep their ON status for the first several days and also convert into OFF-SS RGCs at late time points (7 and 14 dpc). (*B*) Representative Ca²⁺ imaging of the same retinal area at different time points in the SOHU glaucoma model demonstrates changes in light-evoked activities of each RGC type. Cells 1, 2, 7, 10, 11, 12, and 13 retain their ON identity, although they may convert from ON-Trans or ON-Sust1 at baseline to ON-Sust2 at late time points (3 and 5 wpi). Cells 3, 4, 5, 6, 8, and 16 convert from OFF-SS at baseline to ON-Sust. Cells 9, 14, and 15 convert from OFF-SS at baseline into NR at 5 wpi.
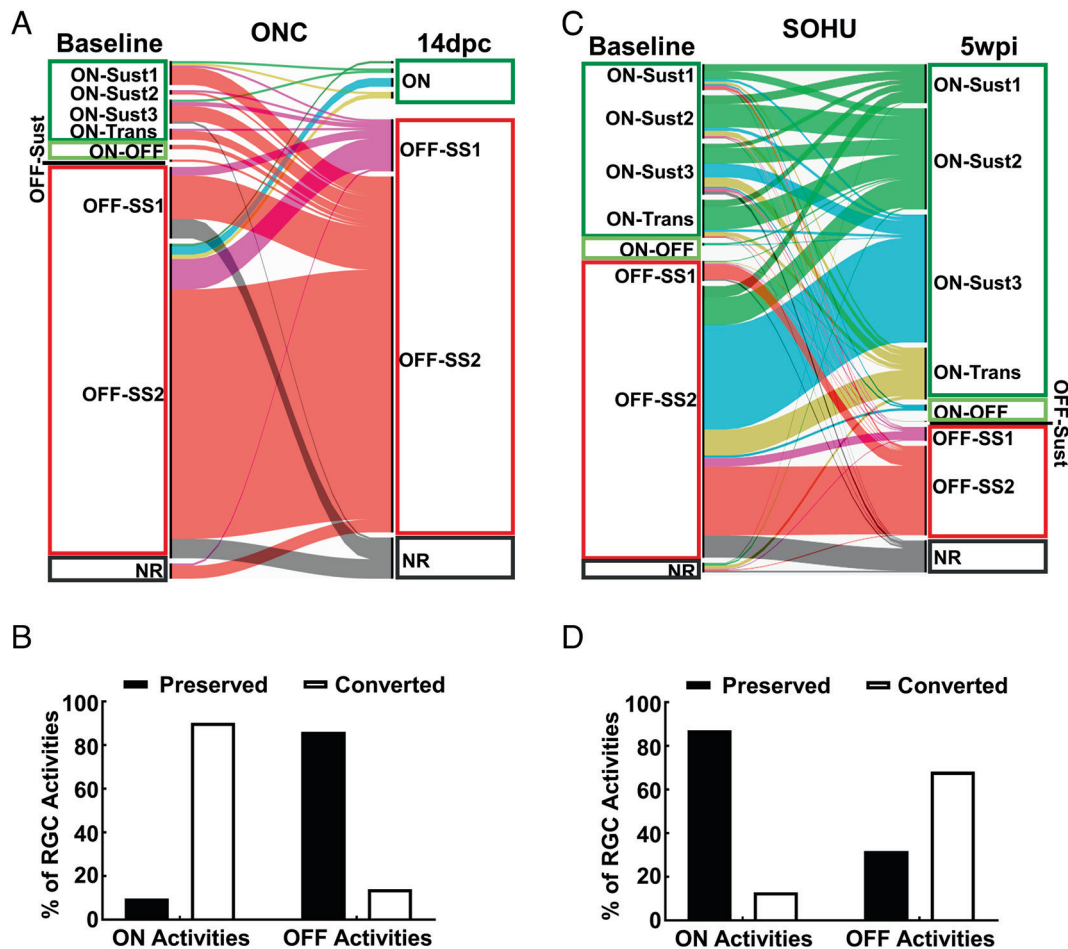
Fig. 6. Quantification of single RGC activity conversion in diseased retinas. (*A* and *C*) Alluvial map showing the original activities of RGCs traced individually (total 217 RGCs in ONC and 534 RGCs in SOHU models) and their final light-evoked activities at 14 dpc or 5 wpi. (*B* and *D*) The percentages of RGCs preserving or changing their original activities in ONC and SOHU retinas.

evoked activities showed ON-RGC conversions by NR (Fig. 5*A*, cells 1, 3, and 15), ON–OFF (Fig. 5*A*, cell 8), and OFF-SS RGCs (Fig. 5*A*, cells 12 and 13) and increased activities of some ON-RGCs (Fig. 5*A*, cells 2, 5, 9, and 14). These changes were consistent with the demonstration by bulk analysis of increased numbers and total activities of ON-RGCs at early time points after ONC (Figs. 4 and *SI Appendix,* Fig. S4). However, most RGCs ultimately converted into OFF-SS RGCs at later time points 7 and 14 dpc (Figs. 5*A* and 6 *A* and *B*). Unlike ONC, glaucomatous ON-RGCs generally retained their original activities in the SOHU model, although they may have converted from ON-Trans or ON-Sust1 at baseline to ON-Sust2 at late time points (3 and 5 wpi), such as cells 1, 2, 7, 10, 11, 12, and 13 in Fig. 5*B*. Also unlike ONC, glaucomatous OFF-SS RGCs tended to convert into ON-RGCs (Fig. 6 *C* and *D*): cells 3, 4, 5, 6, 8, and 16, for example, converted from OFF-SS at baseline to ON-Sust at 5 wpi (Fig. 5*B*). A phenomenon common to both ONC and SOHU glaucoma was that almost no RGCs surviving at late time points (only 1 of 217 RGCs at 14 dpc and 0 of 534 RGCs at 5 wpi) were originally OFF-Trans or OFF-Sust. Thus, OFF-Trans and OFF-Sust RGCs were the most susceptible to trauma and glaucoma consistent with our bulk analysis (*SI Appendix,* Fig. S4) and previous reports that OFF-RGCs are the RGC type most vulnerable to degeneration (66, 67).

We detected significant loss and shrinkage of RGC neurites at 14 dpc in the ONC model (*SI Appendix,* Fig. S6 *A* and *B*), which may have contributed to the ON-to-OFF conversion of crushed

RGCs. In contrast, glaucomatous RGCs preserved neurites relatively well and significantly better than after crush (*SI Appendix,* Fig. S6 *A–C*). Shrinkage of RGC dendrites after ONC and IOP elevation has been reported before (42, 66, 67). This contraction would be consistent with changes in RGC receptive fields and therefore alter their activity. Taken together, these results showed that longitudinal single-cell analysis of in vivo Ca^{2+} imaging is a powerful investigative tool that revealed surprising and unique RGC activity conversion patterns in response to traumatic injury and glaucoma.

Discussion

Only Longitudinal Single-RGC Imaging and Tracing can Reveal Dynamic Transformation of RGC Activity in Response to Injury and Disease. Ex vivo characterization of RGC function is based on snapshots of RGC activities at the moment of testing and assumes that their light-evoked responses remain stable and static. We found this to be valid in normal mice in vivo because longitudinal RGC Ca^{2+} imaging and single-RGC tracing did not detect significant changes of light-evoked RGC activities over time (Fig. 3). It is remarkable, however, that the light-evoked neuronal activities of RGCs continue to change at the population level as disease progresses (Figs. 4 and *SI Appendix,* Fig. S4). Also surprising, and extremely intriguing, the light-evoked activity pattern of individual RGCs continues to transform as an injury or disease evolves (Figs. 5 and 6). This study presents a complete, dynamic view of the same RGCs at different stages or conditions

over time and demonstrates the power of longitudinal tracing of individual RGC Ca^{2+} imaging. Intrinsic and extrinsic changes in RGCs during diseases, including activation/inhibition of endogenous signaling pathways, variations in gene expression, extension/shrinking of neurites, formation/loss of synapses, and potential changes in other non-RGC retinal cells, can significantly alter retinal visual circuits and RGC receptive fields and therefore convert RGC activities. The unique transformations in the patterns of RGC activity associated with trauma and glaucoma may result from one or more of these factors but clearly depend on the specific pathophysiological conditions. Future studies can build on the foundation that we have established and begin to correlate longitudinal analysis of single RGC function, morphology, metabolism, and gene expression. These investigations will generate a more comprehensive understanding of the molecular mechanisms of RGC activity transformation in response to injuries, diseases, and treatments.

Dramatic Differences Between the ONC and SOHU Glaucoma Models. ONC is extensively used as a convenient model of optic neuropathy and often as a surrogate glaucoma model. However, our results using noninvasive Ca^{2+} imaging to monitor progressive RGC activity changes as they evolve after disease and injury suggest that mechanical axon injury and ocular hypertension cause distinct RGC responses: 1) ONC causes an initial increase in ON activities, which subsequently decrease significantly and are almost totally lost at later time points. In contrast, ocular hypertension causes a much milder and slower decrease in total RGC activities, but both ON- and OFF-RGC responses are preserved quite well. 2) Most RGCs convert to OFF-SS RGCs after ONC injury, whereas most ON-RGCs retain their ON identity in the SOHU glaucoma model. 3) There is far greater neurite loss in crushed RGCs than in glaucomatous RGCs. This difference is likely to be at least partly responsible for the distinct RGC responses to these two optic neuropathies. The transcriptomic changes of traumatic RGCs and glaucomatous RGCs are also consistently very different (65), and the susceptibility of RGC subtypes to different injuries varies significantly (68, 69). Taken together, the results of the present study show significant differences in the functional and morphological responses of RGCs after ONC and glaucoma and suggest that the ONC model may not be ideal for studying glaucomatous neurodegeneration.

In Vivo Imaging of RGC Activities Provides an Initial but Compelling Demonstration of Proof of Concept. In glaucoma research, longitudinal assessment of RGC functional deficits and recovery during disease and treatment is critical to evaluate disease progression and efficacies of therapies. The unmet need for this information motivated us to develop in vivo RGC Ca^{2+} imaging assays to longitudinally characterize the dynamic activity changes of RGCs at both bulk and single-cell levels in animal models that can be rigorously controlled. By taking advantage of the superb optical accessibility of the retina and the power of cSLO–retina fundus imaging, we developed in vivo RGC imaging assays to capture intracellular Ca^{2+} transients, a readout of RGC activity evoked by UV light stimulation under normal and disease conditions. The imaging and data analysis protocols generated through this study (Figs. 1–3) enabled us to longitudinally record ~1,200 RGC light-evoked activities per retina repeatedly in the same living animals. Recording of more than 20,000 naïve mouse RGCs identified nine activity groups. To our knowledge, thousands of RGCs have been detected simultaneously and that distinct RGC activity groups have been defined in vivo under physiological conditions. However, we recognize that there are

obvious differences between the results of studies using in vivo imaging and those using ex vivo electrophysiological techniques. These procedures differ in sensitivity, temporal/spatial resolution, and conditions of light stimulation and adaptation. Therefore, it would be naïve to directly match the in vivo ON/OFF activities of RGCs identified in the present study to the well-established RGC functional types defined by their firing rate/action potentials recorded from individual RGCs in the isolated retina by the patch clamp or MEA (1, 2, 26–28). However, the current results must be interpreted cautiously. Constant background illumination certainly complicates the circumstances of RGC activation, and full-field UV light stimulation with high intensity and long duration may generate artifacts by strongly activating the inhibitory surrounding receptive fields. Therefore, the phenotypes that we acquired are based on and restricted by the imaging conditions of our particular in vivo settings, and we can only compare and relate our results to those of studies using similar settings. The same caveat applies to the dynamic changes of individual RGCs in response to light stimulation under disease conditions, which have never been appreciated before; we must be cautious because these changes were detected under the current optical settings. We also want to emphasize that we are measuring the calcium signal, not the actual electrical signal. For example, the long-lasting elevation of intracellular calcium after offset of the stimulating light in ON-Sust1 cells (Fig. 2A) may not precisely reflect neuronal activities, although a newly identified retinal interneuron, the Campana cell, also presents prolonged Ca^{2+} responses (30 s) after very short light stimulation (10 ms) (70). The reliability and precision of in vivo RGC neuronal activities need conclusive confirmation by in vivo study of RGC electrophysiology, applying techniques such as epiretinal-implantable MEA (25, 71). While the present results await this type of definitive confirmation, in vivo RGC Ca^{2+} imaging has enabled us to establish a baseline of RGC activities in response to light stimulation through population recording. This direct measurement of light-evoked RGC activities is: 1) high throughput with single-cell resolution and 2) suitable for longitudinal, repetitive use *in vivo*. Therefore, in vivo Ca^{2+} imaging is precise enough for high-fidelity longitudinal monitoring of population and individual RGC physiological activities and pathological deficits. We expect the evident success of the present proof-of-concept investigation to encourage additional in vivo studies of RGC function. Such imaging will reveal functional/activity biomarkers for various optic neuropathies and other CNS neurodegenerative diseases associated with RGC degeneration (6) and therefore facilitate evaluation of the efficacy of neuroprotective and regenerative therapies. Recently, in vivo Ca^{2+} imaging has recorded a similar scale of visual-evoked neuronal activities in the mouse primary visual cortex (37). It would be extremely interesting to simultaneously image both RGCs and visual cortex neurons and determine the correlation between their activities in response to visual stimuli.

An additional benefit of this technique will be to reduce the number of animals required for experiments; we will be able to study the same animal at a microscopic scale at multiple time points instead of using separate groups of animals for each time point. Furthermore, the ability to follow the very same cellular structures over time will eliminate inconsistencies found in studies that compare different animals at different time points.

The OFF-Sustained Suspect RGCs. We identified a substantial number of RGCs (31.4%) that rapidly decrease their intracellular Ca^{2+} levels in response to UV light stimulation and increase them immediately after offset but have high baseline activities (Fig. 2). This type of OFF-RGCs has been described previously in an ex

vivo electrophysiological study (72). We designated them OFF-Sustained Suspects 1 and 2 to indicate their OFF-Sustained–like responses and to differentiate them from classical OFF-Transient and OFF-Sustained RGCs. Some OFF-Sustained αRGCs indeed have a high baseline firing rate to steady illumination (33). A previous study also presented a group of RGCs with similar Ca^{2+} responses to full-field light stimulation in their Fig. 2*A*, although they named them "OFF-Suppression" RGCs (39). This type of RGCs was also routinely identified by an AO imaging system in the retinas of both mouse (41 of 60 RGCs) (44) and nonhuman primate (7 of 98 RGCs) (73). Detection of these OFF-SS RGCs in vivo may be due to an artifact caused by 488-nm imaging light-evoked photoreceptor responses. However, in an earlier study using a two-photon (2P) AO microscope to minimize photoreceptor activation from imaging light (74), one of the two illustrated RGCs (cell 1 in their Fig. 2*f*) clearly has a downward Ca^{2+} suppression response to blue light stimulation, although the duration of the stimulating blue light was too brief (10 ms) to fully appreciate the dynamic response. At least one prior ex vivo RGC 2P-Ca^{2+} imaging study also detected similar RGCs (39). The evidence from previous studies supports our present finding that this type of OFF-SS RGCs is present in living animals. Another possibility is that these groups of cells are actually ON-center cells with antagonistic surround receptive field. Full-field UV stimulation may increase suppressive effects of the inhibitory surround receptive field and therefore decrease the ON-center response, but offset of the UV light allows the ON-center response to return to baseline. After injury and glaucoma, the dramatically different changes of dendrites and cell coverage in the retina (*SI Appendix*, Fig. S6) can significantly affect both center and surround receptive fields of surviving RGCs and consequently lead to different transformations of functional responses. But how exactly the receptive field of individual RGCs changes in response to different injuries/diseases needs more precise mapping, which requires more advanced in vivo imaging/visual stimulation setting, as we discuss below.

Future Improvements of the Current Imaging Setup. The present in vivo RGC analysis should be considered preliminary because of limitations of the current imaging setup. These include: 1) the 488-nm excitation light, which can also activate photoreceptors, thus contaminating UV stimulation of RGCs; 2) the paucity of visual stimuli from which those for spot and white noise (*vs.* full-field), direction and orientation selectivity, and temporal/contrast/chromatic discrimination are missing and which would allow more specific and accurate analysis of RGC functional type; and 3) the lack of additional fluorescence channels, which would allow use of molecular markers, and of multisensor simultaneous detection. Future incorporation of a 2P excitation laser into cSLO (75–77) will allow invisible infrared light to be used for GECI excitation and minimize activation of photoreceptors by excitation light. This improvement will make it possible to use visible light with static and moving spot or bars to specifically stimulate rods, cones, or both and to acquire fully the spectrum of RGC activities, especially those of direction-selective RGCs that we currently cannot appreciate. If an additional fluorescence channel can be incorporated into the cSLO, it will be possible to use one channel to label RGC subtypes by defining molecular markers (1) and the other to identify visual-evoked activities and thus to link RGC activity to molecular-defined RGC types. Because genetically encoded voltage indicators (GEVIs), which directly measure electrical activity of neurons with submillisecond resolution (78, 79), are more precise than GECIs, incorporating them into a cSLO equipped with an ultrafast camera will allow the actual electrophysiological characteristics of RGCs to be detected directly in vivo. Additionally, use of transgenic mice with more uniform and stable expression of less toxic advanced GECI/GEVI in RGCs specifically would reduce sampling bias against RGCs dimly labeled or lost by GECI toxicity.

In summary, our present results demonstrate the feasibility of directly visualizing light-evoked RGC activities and develop and validate the powerful analytic strategies that make such studies possible. Importantly, they also therefore establish the foundation for numerous highly informative in vivo studies in the future. Among the investigations now possible are in vivo classification of RGC functional type, comparison of RGC activity in diverse optic neuropathies and other CNS neurodegeneration diseases with RGC/ON-related symptoms, and advanced in vivo imaging analysis of neuronal morphological and metabolic changes in response to illness and therapies. The current studies reveal distinctive susceptibilities and dynamic functional conversion of individual RGCs in response to traumatic and glaucomatous injuries. These features of in vivo activity have never been appreciated before, and it will be scientifically fascinating and clinically important to determine whether this diversity of reaction, especially the activity conversion, is a universal characteristic shared by other neuronal cell types in response to injury and diseases. Our results demonstrate the potential of in vivo RGC Ca^{2+} imaging as a reliable, sensitive, direct, and noninvasive RGC functional measurement at the single-cell level but with high-throughput capability. This type of assessment is desperately needed for both basic and translational research to identify the much-sought functional biomarkers for early detection and longitudinal monitoring of glaucomatous degeneration and to assess the functional recovery of protected/regenerated/transplanted RGCs. The strategy will be readily translated to clinical application once safer and sensitive Ca^{2+}/voltage dyes become available in the future.

Materials and Methods

Statistical Analyses. Ca^{2+} activity heatmap was generated by MATLAB. Alluvial maps of the conversion of RGC types were generated by R program. GraphPad Prism 6 was used to generate graphs and for statistical analyses. Data are presented as means ± SEM. Student's *t* test was used for two-group comparison, and one-way ANOVA with the post hoc test was used for multiple comparisons.

All reagents and detailed procedures are provided in *SI Appendix*.

Author affiliations: aSpencer Center for Vision Research, Department of Ophthalmology, Byers Eye Institute at Stanford University School of Medicine, Palo Alto, CA 94304; bDepartment of Ophthalmology, The Second Xiangya Hospital, Central South University, Changsha 410011, China; cDepartment of Biomedical Engineering, Northwestern University, Evanston, IL 60208; and dDepartment of Ophthalmology, University of California San Francisco, San Francisco, CA 94143

1. J. R. Sanes, R. H. Masland, The types of retinal ganglion cells: Current status and implications for neuronal classification. *Annu. Rev. Neurosci.* **38**, 221–246 (2015).
2. S. Wienbar, G. W. Schwartz, The dynamic receptive fields of retinal ganglion cells. *Prog. Retin. Eye. Res.* **67**, 102–117 (2018).
3. L. A. Levin, Mechanisms of optic neuropathy. *Curr. Opin. Ophthalmol.* **8**, 9–15 (1997).
4. C. F. Burgoyne, A biomechanical paradigm for axonal insult within the optic nerve head in aging and glaucoma. *Exp. Eye Res.* **93**, 120–132 (2011).
5. A. DeBusk, M. L. Moster, Gene therapy in optic nerve disease. *Curr. Opin. Ophthalmol.* **29**, 234–238 (2018).
6. V. Carelli, C. La Morgia, F. N. Ross-Cisneros, A. A. Sadun, Optic neuropathies: The tip of the neurodegeneration iceberg. *Hum. Mol. Genet.* **26**, R139–R150 (2017).
7. Y. C. Tham *et al.*, Global prevalence of glaucoma and projections of glaucoma burden through 2040: A systematic review and meta-analysis. *Ophthalmology* **121**, 2081–2090 (2014).
8. D. J. Calkins, Adaptive responses to neurodegenerative stress in glaucoma. *Prog. Retin. Eye Res.* **84**, 100953 (2021), 10.1016/j.preteyeres.2021.100953, 100953.
9. R. A. Russell, D. P. Crabb, R. Malik, D. F. Garway-Heath, The relationship between variability and sensitivity in large-scale longitudinal visual field data. *Invest. Ophth. Vis. Sci.* **53**, 5985–5990 (2012).
10. P. H. Artes, A. Iwase, Y. Ohno, Y. Kitazawa, B. C. Chauhan, Properties of perimetric threshold estimates from full threshold, SITA standard, and SITA fast strategies. *Invest. Ophth. Vis. Sci.* **43**, 2654–2659 (2002).
11. D. C. Hood, R. H. Kardon, A framework for comparing structural and functional measures of glaucomatous damage. *Prog. Retin Eye Res.* **26**, 688–710 (2007).
12. D. C. Hood, S. C. Anderson, M. Wall, A. S. Raza, R. H. Kardon, A test of a linear model of glaucomatous structure-function loss reveals sources of variability in retinal nerve fiber and visual field measurements. *Invest. Ophthalmol. Vis. Sci.* **50**, 4254–4266 (2009).
13. P. H. Artes, D. M. Hutchison, M. T. Nicolela, R. P. LeBlanc, B. C. Chauhan, Threshold and variability properties of matrix frequency-doubling technology and standard automated perimetry in glaucoma. *Invest. Ophthalmol. Vis. Sci.* **46**, 2451–2457 (2005).
14. S. K. Gardiner, W. H. Swanson, D. Goren, S. L. Mansberger, S. Demirel, Assessment of the reliability of standard automated perimetry in regions of glaucomatous damage. *Ophthalmology* **121**, 1359–1369 (2014).
15. C. G. de Moraes, J. M. Liebmann, F. A. Medeiros, R. N. Weinreb, Management of advanced glaucoma: Characterization and monitoring. *Survey of ophthalmol.* **61**, 597–615 (2016).
16. V. Porciatti, Electrophysiological assessment of retinal ganglion cell function. *Exp. Eye Res.* **141**, 164–170 (2015).
17. T. H. Chou, J. Bohorquez, J. Toft-Nielsen, O. Ozdamar, V. Porciatti, Robust mouse pattern electroretinograms derived simultaneously from each eye using a common snout electrode. *Invest Ophthalmol Vis Sci* **55**, 2469–2475 (2014).
18. T. H. Chou, V. Porciatti, The bioelectric field of the pattern electroretinogram in the mouse. *Invest. Ophthalmol. Vis. Sci.* **53**, 8086–8092 (2012).
19. T. H. Chou, K. K. Park, X. Luo, V. Porciatti, Retrograde signaling in the optic nerve is necessary for electrical responsiveness of retinal ganglion cells. *Invest. Ophthalmol. Vis. Sci.* **54**, 1236–1243 (2013).
20. L. Li *et al.*, Longitudinal morphological and functional assessment of RGC neurodegeneration after optic nerve crush in mouse. *Front. Cell. Neurosci.* **14**, 109 (2020).
21. J. Zhang *et al.*, Silicone oil-induced ocular hypertension and glaucomatous neurodegeneration in mouse. *eLife* **8**, e45881 (2019).
22. Y. Zhang *et al.*, In vivo evaluation of retinal ganglion cells and optic nerve's integrity in large animals by multi-modality analysis. *Exp. Eye Res.* **197**, 108117 (2020).
23. J. Zhang *et al.*, A reversible silicon oil-induced ocular hypertension model in mice. *J. Visualized Exp. JoVE* (2019).
24. F. Fang *et al.*, Chronic mild and acute severe glaucomatous neurodegeneration derived from silicone oil-induced ocular hypertension. *Sci. Rep.* **11**, 9052 (2021).
25. N. M. Tran *et al.*, Single-cell profiles of retinal ganglion cells differing in resilience to injury reveal neuroprotective genes. *Neuron* **104**, 1039–1055.e12 (2019), 10.1016/j.neuron.2019.11.006.
26. E. J. Chichilnisky, R. S. Kalmar, Functional asymmetries in ON and OFF ganglion cells of primate retina. *J. Neurosci.* **22**, 2737–2747 (2002).
27. M. Fiscella *et al.*, Recording from defined populations of retinal ganglion cells using a high-density CMOS-integrated microelectrode array with real-time switchable electrode selection. *J. Neurosci. Met.* **211**, 103–113 (2012).
28. G. D. Field *et al.*, Functional connectivity in the retina at the resolution of photoreceptors. *Nature* **467**, 673–677 (2010).
29. S. Sabbah *et al.*, A retinal code for motion along the gravitational and body axes. *Nature* **546**, 492–497 (2017).
30. O. S. Dhande *et al.*, Genetic dissection of retinal inputs to brainstem nuclei controlling image stabilization. *J. Neurosci.* **33**, 17797–17813 (2013).
31. A. Nath, G. W. Schwartz, Electrical synapses convey orientation selectivity in the mouse retina. *Nat. commun.* **8**, 2025 (2017).
32. J. J. Pang, F. Gao, S. M. Wu, Light-evoked excitatory and inhibitory synaptic inputs to ON and OFF alpha ganglion cells in the mouse retina. *J. Neurosci.* **23**, 6063–6073 (2003).
33. B. Krieger, M. Qiao, D. L. Rousso, J. R. Sanes, M. Meister, Four alpha ganglion cell types in mouse retina: Function, structure, and molecular signatures. *PLoS One* **12**, e0180091 (2017).
34. J. Jacoby, G. W. Schwartz, Three small-receptive-field ganglion cells in the mouse retina are distinctly tuned to size, speed, and object motion. *J. Neurosci.* **37**, 610–625 (2017).
35. M. Z. Lin, M. J. Schnitzer, Genetically encoded indicators of neuronal activity. *Nat. Neurosci.* **19**, 1142–1153 (2016).
36. L. Tian *et al.*, Imaging neural activity in worms, flies and mice with improved GCaMP calcium indicators. *Nat. Met.* **6**, 875–881 (2009).
37. O. I. Rumyantsev *et al.*, Fundamental bounds on the fidelity of sensory cortical coding. *Nature* **580**, 100–105 (2020).
38. Q. Chen *et al.*, Imaging neural activity using Thy1-GCaMP transgenic mice. *Neuron* **76**, 297–308 (2012).
39. T. Baden *et al.*, The functional diversity of retinal ganglion cells in the mouse. *Nature* **529**, 345–350 (2016).
40. A. C. Weitz *et al.*, Imaging the response of the retina to electrical stimulation with genetically encoded calcium indicators. *J. Neurophysiol.* **109**, 1979–1988 (2013).
41. B. C. Chauhan *et al.*, Longitudinal in vivo imaging of retinal ganglion cells and retinal thickness changes following optic nerve injury in mice. *PLoS One* **7**, e40352. (2012).
42. C. K. Leung *et al.*, Long-term in vivo imaging and measurement of dendritic shrinkage of retinal ganglion cells. *Invest. Ophthalmol. Vis. Sci.* **52**, 1539–1547 (2011).
43. C. A. Smith, B. C. Chauhan, Imaging retinal ganglion cells: Enabling experimental technology for clinical application. *Prog. Retin Eye Res.* **44**, 1–14 (2015).
44. L. Yin *et al.*, Imaging light responses of retinal ganglion cells in the living mouse eye. *J. Neurophysiol.* **109**, 2415–2421 (2013).
45. S. K. Cheong, J. M. Strazzeri, D. R. Williams, W. H. Merigan, All-optical recording and stimulation of retinal neurons in vivo in retinal degeneration mice. *PLoS One* **13**, e0194947 (2018).
46. H. Dana *et al.*, High-performance calcium sensors for imaging activity in neuronal populations and microcompartments. *Nat. Met.* **16**, 649–657 (2019).
47. L. Yang *et al.*, The mTORC1 effectors S6K1 and 4E-BP play different roles in CNS axon regeneration. *Nat. commun.* **5**, 5416 (2014).
48. L. Miao *et al.*, mTORC1 is necessary but mTORC2 and GSK3beta are inhibitory for AKT3-induced axon regeneration in the central nervous system. *eLife* **5**, e14908 (2016).
49. H. Huang *et al.*, AKT-dependent and -independent pathways mediate PTEN deletion-induced CNS axon regeneration. *Cell Death Dis.* **10**, 203 (2019).
50. Q. Wang *et al.*, Mouse gamma-synuclein promoter-mediated gene expression and editing in mammalian retinal ganglion cells. *J. Neurosci.* **40**, 3896–3914 (2020).
51. Y. V. Wang, M. Weick, J. B. Demb, Spectral and temporal sensitivity of cone-mediated responses in mouse retinal ganglion cells. *J. Neurosci.* **31**, 7670–7681 (2011).
52. G. H. Jacobs, J. Neitz, J. F. Deegan 2nd, Retinal receptors in rodents maximally sensitive to ultraviolet light. *Nature* **353**, 655–656 (1991).
53. S. S. Nikonov, R. Kholodenko, J. Lem, E. N. Pugh Jr., Physiological features of the S- and M-cone photoreceptors of wild-type mice from single-cell recordings. *J. general physiol.* **127**, 359–374 (2006).
54. F. M. Nadal-Nicolas *et al.*, True S-cones are concentrated in the ventral mouse retina and wired for color detection in the upper visual field. *eLife* **9**, e56840 (2020).
55. T. Baden *et al.*, A tale of two retinal domains: Near-optimal sampling of achromatic contrasts in natural scenes through asymmetric photoreceptor distribution. *Neuron* **80**, 1206–1217 (2013).
56. H. Zou, T. Hastie, R. Tibshirani, Sparse principal component analysis. *J. Comput. Graphical Stat.* **15**, 265–286 (2006).
57. K. Sjöstrand, L. H. Clemmensen, R. Larsen, G. Einarsson, B. Ersbøll, SpaSM: A MATLAB toolbox for sparse statistical modeling. *J. Stat. Software* **84**, (2018).
58. C. Fraley, A. E. Raftery, Model-based clustering, discriminant analysis, and density estimation. *J. Am. Stat. Assoc.* **97**, 611–631 (2002).
59. N. Tian, D. R. Copenhagen, Visual stimulation is required for refinement of ON and OFF pathways in postnatal retina. *Neuron* **39**, 85–96 (2003).
60. J. Jouty, G. Hilgen, E. Sernagor, M. H. Hennig, Non-parametric physiological classification of retinal ganglion cells in the mouse retina. *Front. Cell. Neurosci.* **12**, 481 (2018).
61. C. Stone, L. H. Pinto, Receptive field organization of retinal ganglion cells in the spastic mutant mouse. *J. physiol.* **456**, 125–142 (1992).
62. D. J. Calkins, Critical pathogenic events underlying progression of neurodegeneration in glaucoma. *Prog. Retin. Eye. Res.* **31**, 702–719 (2012).
63. P. Ichhpujani, A. Jindal, L. Jay Katz, Silicone oil induced glaucoma: A review. *Graefe's Arch. Clin. Exp. Ophthalmol.* **247**, 1585–1593 (2009).
64. H. L. Kornmann, S. J. Gedde, Glaucoma management after vitreoretinal surgeries. *Curr. Opin. Ophthal* **27**, 125–131 (2016).
65. J. Wang, F. L. Struebing, E. E. Geisert, Commonalities of optic nerve injury and glaucoma-induced neurodegeneration: Insights from transcriptome-wide studies. *Exp. Eye Res.* **207**, 108571 (2021).
66. R. N. El-Danaf, A. D. Huberman, Characteristic patterns of dendritic remodeling in early-stage glaucoma: Evidence from genetically identified retinal ganglion cell types. *J. Neurosci.* **35**, 2329–2343 (2015).
67. Y. Ou, R. E. Jo, E. M. Ullian, R. O. Wong, L. Della Santina, Selective vulnerability of specific retinal ganglion cell types and synapses after transient ocular hypertension. *J. Neurosci.* **36**, 9240–9252 (2016).
68. I. Christensen *et al.*, The susceptibility of retinal ganglion cells to glutamatergic excitotoxicity is type-specific. *Front Neurosci.* **13**, 219 (2019).
69. N. Yang, B. K. Young, P. Wang, N. Tian, The susceptibility of retinal ganglion cells to optic nerve injury is type specific. *Cells* **9**, 677 (2020).
70. B. K. Young *et al.*, An uncommon neuronal class conveys visual signals from rods and cones to retinal ganglion cells. *Proc. Natl. Acad. Sci. U.S.A.* **118**, e2104884118 (2021).

71. G. Hong *et al.*, A method for single-neuron chronic recording from the retina in awake mice. *Science* **360**, 1447–1451 (2018).
72. J.-J. Pang, F. Gao, S. M. Wu, Light-evoked excitatory and inhibitory synaptic inputs to ON and OFF α ganglion cells in the mouse retina. *J. Neuroscience* **23**, 6063–6073 (2003).
73. L. Yin *et al.*, Imaging light responses of foveal ganglion cells in the living macaque eye. *J. Neurosci.* **34**, 6596–6605 (2014).
74. Z. Qin *et al.*, Adaptive optics two-photon microscopy enables near-diffraction-limited and functional retinal imaging in vivo. *Light Sci. Appl.* **9**, 79 (2020).
75. T. Kamali, S. R. M. Farrell, W. H. Baldridge, J. Fischer, B. C. Chauhan "Two-photon scanning laser ophthalmoscope" in *High Resolution Imaging in Microscopy and Ophthalmology: New Frontiers in Biomedical Optics*, J. F. Bille, Ed. (Springer, Cham (CH), 2019), pp. 195–211, 10.1007/978-3-030-16638-0_9.
76. R. Sharma *et al.*, In vivo two-photon imaging of the mouse retina. *Biomed. Opt. Express* **4**, 1285–1293 (2013).
77. A. S. Bar-Noam, N. Farah, S. Shoham, Correction-free remotely scanned two-photon in vivo mouse retinal imaging. *Light Sci. Appl.* **5**, e16007 (2016).
78. V. Villette *et al.*, Ultrafast two-photon imaging of a high-gain voltage indicator in awake behaving mice. *Cell* **179**, 1590–1608.e1523 (2019).
79. J. Wu *et al.*, Kilohertz two-photon fluorescence microscopy imaging of neural activity in vivo. *Nat. Met.* **17**, 287–290 (2020).